Reynolds number scaling of flow in a Rushton turbine stirred tank. Part I—Mean flow, circular jet and tip vortex scaling

H.S. Yoon[a], D.F. Hill[b], S. Balachandar[c],*, R.J. Adrian[c], M.Y. Ha[a]

[a]*School of Mechanical Engineering, Pusan National University, San 30 Chang Jeon Dong, South Korea*
[b]*Department of Civil & Environmental Engineering, Pennsylvania State University, 212 Sackett Building, University Park, PA, 16802, USA*
[c]*Department of Theoretical & Applied Mechanics, 216 Talbot Laboratory, University of Illinois at Urbana-Champaign, NC-262,
104 South Wright Street, Urbana, IL, 61801 2983, USA*

Abstract

We consider scaling of flow within a stirred tank with increasing Reynolds number. Experimental results obtained from two different tanks of diameter 152.5 and 292.1 mm, with a Rushton turbine operating at a wide range of rotational speeds stirring the fluid, are considered. The Reynolds number ranges from 4000 to about 78,000. Phase-locked stereoscopic PIV measurements on three different vertical planes close to the impeller give phase-averaged mean flow on a cylindrical surface around the impeller. The scaling of θ- and plane-averaged radial, circumferential and axial mean velocity components is first explored. A theoretical model for the impeller-induced flow is used to extract the strength and size of the three dominant elements of the mean flow, namely the circumferential flow, the jet flow and the pairs of tip vortices. The scaling of these parameters with Reynolds number for the two different tanks is then obtained. The plane-averaged mean velocity scales with the blade tip velocity above a Reynolds number of about 15,000. However, parameters associated with the jet and tip vortices do not become Reynolds number independence until Re exceeds about 10^5. The results for the two tanks exhibit similar Reynolds number dependence, however, a perfect collapse is not observed, suggesting a sensitive dependence of the mean flow to the finer details of the impeller.
© 2005 Published by Elsevier Ltd.

Keywords: Rushton turbine; Turbulence; Mixing; Scaling; Particle image velocimetry

1. Introduction

Scaling of flow and mixing within a stirred tank reactor is of significant practical importance. For lack of a satisfactory understanding, the design of production-scale stirred tanks often evolves through a number of stages that iterate between laboratory experiments and pilot plants, a time-consuming and expensive step-by-step scale-up process. Part of the difficulty is that mean flow and turbulence quantities, such as rms fluctuation and dissipation, often scale differently with increasing tank size and operating speed. As a result the scaling of mixing within the tank can be complex.

The last three decades have seen several high quality experimental measurements of flow inside stirred tanks using modern techniques such as laser doppler anemometry (LDA) and particle image velocimetry (PIV) (Desouza and Pike, 1972; Van't Riet and Smith, 1975; van der Molen and van Maanen, 1978; Kolar et al., 1984; Costes and Couderc, 1988; Dong et al., 1994; Sturesson et al., 1995; Stoots and Calabrese, 1995; Ducoste et al., 1997; Kemoun et al., 1998; Lamberto et al., 1999; Montante et al., 1999; Mahouast et al., 1989; Schaffer et al., 1997; Derksen et al., 1999; Escudie and Line, 2003; Escudie et al., 2004). In particular, several of these experimental investigations have considered flow and mixing inside stirred tanks of varying size operating over a range of speeds and, thus, have addressed, directly or indirectly, the scaling of mean and turbulence quantities

* Corresponding author. Tel.: +1 217 244 4371; fax: +1 217 244 9090.
E-mail address: s-bala@uiuc.edu (S. Balachandar).

with Reynolds number (Desouza and Pike, 1972; Van't Riet and Smith, 1975; van der Molen and van Maanen, 1978; Kolar et al., 1984; Costes and Couderc, 1988; Dong et al., 1994; Sturesson et al., 1995; Stoots and Calabrese, 1995; Ducoste et al., 1997; Kemoun et al., 1998; Lamberto et al., 1999; Montante et al., 1999). These studies together cover a wide range of Reynolds number from 10 to 1.2×10^5, where Reynolds number is defined in terms of impeller blade-tip diameter, D, and the number of blade rotations per second, N, as $Re = ND^2/\nu$ (ν is the kinematic viscosity of the fluid). However, the range of Re considered in each investigation is limited. At higher Reynolds numbers relevant to turbulent flow, the overall time-averaged mean flow and rms turbulent fluctuations appear to scale with the impeller blade-tip velocity.

Costes and Couderc (1988) have addressed the problem of scaling of mean flow and turbulence using two different sized tanks over three different Reynolds numbers. Their results suggest that velocity statistics such as, mean, rms, spectra and autocorrelation scale with the blade-tip velocity. However, higher order turbulence statistics, such as dissipation, do not show complete collapse when scaled appropriately in terms of impeller diameter and rotation rate. The results of Stoots and Calabrese (1995) on deformation rate over a Reynolds number range of 29,200–45,800, however, show a reasonable Reynolds number independence when nondimensionalized by the inverse time scale.

van der Molen and van Maanen (1978) emphasized the importance of blade-tip trailing vortices. They pointed out that the time-averaged flow in the laboratory frame of reference (as measured by a fixed probe) averages out the influence of tip vortices as they sweep past the probe along with the blades. The resulting time-averaged mean flow was observed to scale well with the blade-tip velocity. The effect of tip vortex pairs was carefully isolated through phase-average, and the tip vortex strength did not scale perfectly with blade-tip velocity. Some dependence on tank size was observed. Van't Riet and Smith (1975) also investigated the scaling of blade-tip vortices over a wide Reynolds number range of 300–90,000. The vortex trajectory was observed to be Reynolds number dependent at lower, transitional Reynolds numbers, but Reynolds number independent, within experimental uncertainty, above a Reynolds number of 15,000. Other quantities such as vortex strength, when appropriately scaled, also tended towards Reynolds number independence at higher Reynolds numbers.

In spite of the above efforts the scaling of flow and mixing within a stirred tank with increasing tank size and impeller speed remains not fully understood. In this paper, we address the question of scaling with experiments performed in two different tanks with impeller speed varying over Reynolds numbers ranging from 4000 to 80,000. The two tanks were constructed to be geometrically similar. Both employ a lid at the top of the tank in order to prevent free surface (Froude number) effects. The flow is entirely driven by the rotating impeller and the operational speeds are such that Mach and Rossby numbers are irrelevant. Reynolds number is expected to be the only relevant parameter of the problem. The results for each tank, when appropriately nondimensionalized by the blade tip radius and velocity, show Reynolds number independence with increasing impeller speed at sufficiently high Reynolds number. However, surprisingly the results for the two different tanks do not exhibit a perfect collapse, suggesting sensitive dependence on small differences, especially in the geometric scaling of their impellers.

Stereoscopic PIV measurements were made on three different vertical planes within the tank. The instantaneous measurements are phase-locked with the blade position and ensemble averaging over many such realizations yields the phase-averaged mean velocity. The measurement on the three planes, which are located close to the impeller swept volume, are interpolated to obtain all three components of the phase-averaged mean velocity on a cylindrical plane of constant radius located just beyond the impeller tip. The velocity on this cylindrical plane is the impeller-induced inflow and it can be considered to dictate the flow over the entire tank at large (Yoon et al., 2002). Thus, here we consider the scaling of velocity measured over this plane as a proxy for scaling of flow over the entire stirred tank.

The phase-averaged mean flow within the tank stirred with a Rushton turbine can be considered to be made up of three different basic flow elements: circumferential flow, a jet flow and pairs of tip vortices associated with the impeller blades. This simple decomposition has been shown to be effective in modeling the impeller induced flow, particularly in the neighborhood of the impeller (see Yoon et al., 2001). Here we investigate the scaling of each of these elements individually with increasing tank size and impeller rotation rate. By looking at the scaling of parameters, such as the strength and size of the jet and tip vortex pairs individually, we hope to address the question of mean flow scaling in more detail. In particular, it is of interest to establish the minimum Reynolds number necessary for these parameters to be Reynolds number independent.

Here we will also investigate the scaling of both vorticity and dissipation for the two tanks and in particular, address when they become Reynolds number independent. If the scaling of the mean flow were to be uniform over the entire tank, we expect the scaling of these higher order quantities to follow that of the mean flow. However, it can be anticipated that the Reynolds number independence of the nondimensional vorticity and dissipation will be delayed to much higher Reynolds numbers, since these derivative quantities give more importance to the smaller scales of motion. Thus, the results on the scaling of vorticity and dissipation can be used to interpret the scale-dependence of mean flow scaling. The present work is limited to investigation of only the scaling of velocity field. Practical factors relevant to industrial mixing such as mixing time, heat and mass transfer, and multiphase flow are not considered in this study. However, the scaling properties of the flow to be discussed here will likely have an effect on these additional complex processes.
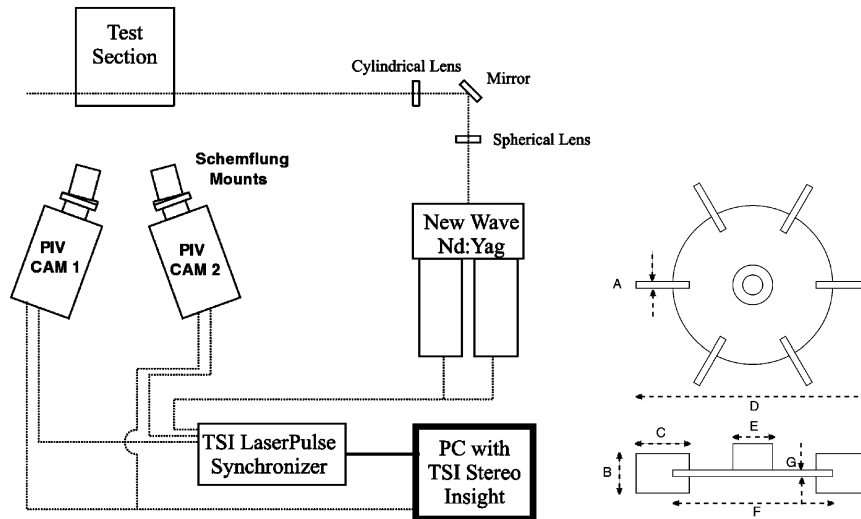
	Small Tank (in mm)	Large Tank (in mm)	Ratio
T	152.5	292.1	1.92
A	2.19	3.53	1.61
B	10.28	19.54	1.9
C	12.37	24.50	1.98
D	50.59	97.20	1.92
E	12.51	15.98	1.28
F	33.16	63.20	1.91
G	2.40	3.44	1.43

Fig. 1. Overhead schematic of experimental apparatus and data acquisition system.

2. Experimental methodology

2.1. Apparatus

The experiments were an extension of more limited experiments first reported by Hill et al. (2000). A schematic overhead view of the set-up for the current stereoscopic PIV experiments is shown in Fig. 1. To assess the influence of geometric scaling, two geometrically similar test sections were considered. In both cases, an acrylic, unbaffled[1] circular cylinder was mounted within a slightly larger square tank. The diameters of the two circular tanks were $T_1 = 152.5$ cm and $T_2 = 292.1$ cm. The cylinder was filled with de-ionized water to a depth equal to its diameter and the volume between the cylindrical and the square tanks was also filled, in order to reduce the optical distortion due to the curved surface. A lid, with a small hole to accommodate the impeller shaft, was placed on top of the liquid. The purpose of

the lid was to suppress the free-surface displacement, which becomes significant otherwise at higher speeds of impeller rotation. The tolerances between the shaft, lid, and the cylindrical tank were all very tight.

The two tanks were geometrically similar. The lid on top eliminates any free surface and associated Froude number effect. The flow within the tank is completely determined by the impeller rotation and therefore in the present problem the rotational and velocity scales are not independent (Rossby number becomes irrelevant). Furthermore, the velocities considered are quite low that Mach number effect can be ignored. Thus dynamic similarity between the two tanks could be achieved by simply matching the Reynolds numbers. However, some subtle differences in the impellers of the two different arrangements must be noted. The Rushton impeller for the small tank was supplied by Lightnin, Inc., and the impeller for the large tank was custom made by Proprmix, Inc. Fig. 1 also shows the detailed sketch of the impeller geometry with the corresponding measurements for the two tanks. While the diameter of the impeller, blade length, blade height and diameter of the disk were geometrically scaled, the blade thickness, disk thickness, sleeve

---

[1] The use of baffles is a practical means by which to impede the rotation of the fluid. However, one purpose of these experiments was to obtain detailed data for comparison to CFD results, so the simple baffle-free geometry was chosen.
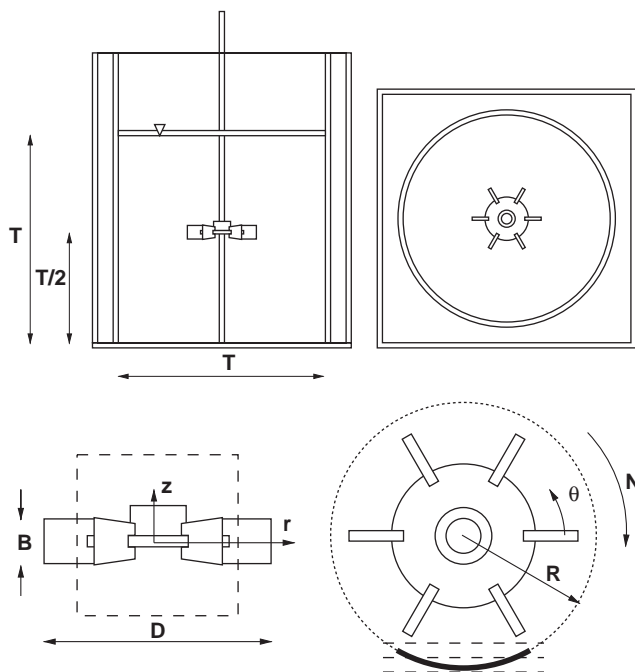
Fig. 2. Side and top view details of the tank and the impeller. Details of the three data acquisition planes and the cylindrical interpolation surface.

Table 1
Rotational speed and Reynolds numbers of experimental data sets

Small tank		Large tank	
Ω (rpm)	$Re = ND^2/v$	Ω (rpm)	$Re = ND^2/v$
100	4293	27	4229
150	6440	41	6421
367	15,756	100	15,662
551	23,655	150	23,492
734	31,512	200	31,323
1102	47,311	300	46,985
1469	63,066	400	62,646
		500	78,308

diameter were not perfectly scaled between the small and large tanks. The ramifications of these seemingly minor differences will be discussed later.

The Rushton turbine was mounted at mid-depth along the axis of the cylinder. The shaft extends through the impeller to the bottom of the tank, where it was held in place by a small nylon sleeve bearing. The bearing eliminated 'wobble' of the impeller. Detailed views of the experimental tank and impeller are shown in Fig. 2. Two different Lightnin Labmaster mixers drove the impellers: the first with a speed range of 50–1800 rpm and the second with a speed range of 20–550 rpm. Details, such as the mounting of the impeller, position of the top lid, etc., for the two tanks are maintained geometrically similar.

The flow was seeded with 8-μm particles from Potters Industries. New-Wave Nd:Yag lasers, operating at ∼ 50 mJ/pulse, illuminated the flow with a light sheet approximately 1 mm thick. Two TSI PIVCAM 10–30 CCD cameras (1 K × 1 K resolution), equipped with Nikon AF MicroNikkor 60 mm lenses, acquired images of the illuminated particles. The included angle between the angularly offset cameras was roughly 45°. Scheimpflug lens mounts were used to reduce the required depth of field and to improve focusing over the field of view. A TSI Laser Pulse Synchronizer and a PC equipped with TSI Stereo Insight software completed the image acquisition package.

2.2. Experimental procedure

Because of the lid, the only upper bounds on impeller speed were those placed by the power and speed limits of

the mixers. As a result, it was possible to cover Reynolds numbers ranging from 4000 to 80,000. Table 1 details the experimental dimensions for both tanks.

As indicated in Fig. 2, data were obtained on three vertical planes located very close to the tips of the impeller blades. An optical encoder, focused on the impeller shaft, was used to trigger acquisition such that the impeller blades were in the position shown for each realization. For the small tank experiments, these planes were located at distances of 23.22, 25.13, and 27.67 mm from the impeller shaft. For the large tank experiments, these planes were located at distances of 45.12, 48.77, and 53.64 mm. For each combination of impeller speed and acquisition plane, an ensemble of 500 realizations was obtained.

The raw images from the left and right cameras were individually interrogated and then validated. Finally, the two two-dimensional vector fields were combined, using a mapping determined by calibration, into a single three-component velocity vector field on a planar surface. The individual data sets were first ensemble averaged to yield a mean velocity field.[2] The mean velocity fields on the three vertical planes for a given rotational speed were then interpolated, using a second-order fit, onto a 60° segment of a cylindrical shell of radius R, as illustrated in Fig. 2. Finally, the Cartesian velocity components were rotated into polar cylindrical coordinates, yielding radial, circumferential and axial velocity components, $\langle u_r \rangle$, $\langle u_\theta \rangle$ and $\langle u_z \rangle$, on the curved cylindrical plane, i.e., for $r = 1.06$, $0 \leqslant \theta \leqslant 60°$ and $-0.6 \leqslant z \leqslant 0.6$ (see Fig. 2 for coordinate definition). Here angle brackets indicate an average over the ensemble. Note that here and in what follows all lengths are nondimensionalized by the blade tip radius ($D/2$) and the velocities have been nondimensionalized by the blade-tip velocity (πND).

---

[2] With regards to the present data, the term "mean flow" denotes phase-averaged flow obtained from the ensemble average of the phase-locked measurement. It is therefore dependent on all three coordinates. Any further space average of the mean flow will be explicitly stated in what follows.

3. Results

3.1. Mean flow scaling

The mean flow ensemble-averaged over all the realizations ($\langle u_r \rangle$, $\langle u_\theta \rangle$, $\langle u_z \rangle$) and interpolated onto the cylindrical surface is shown in Fig. 3 for the small tank at the lowest rotation speed, corresponding to $Re = 4300$. In Fig. 3 frame (a) shows the in-plane velocity vector plot and frame (b) shows the out-of-plane (radial) velocity contours. Only a 60° sector is shown, and the view is limited to the top half of the tank with the region below the center-plane obtained by symmetry. The θ-dependence of the flow field is due to the presence of the tip vortices, whose impact is most evident in the figure around $\theta = 18 \pm 1°$ and $z \approx 0.1 \pm 0.1$. The
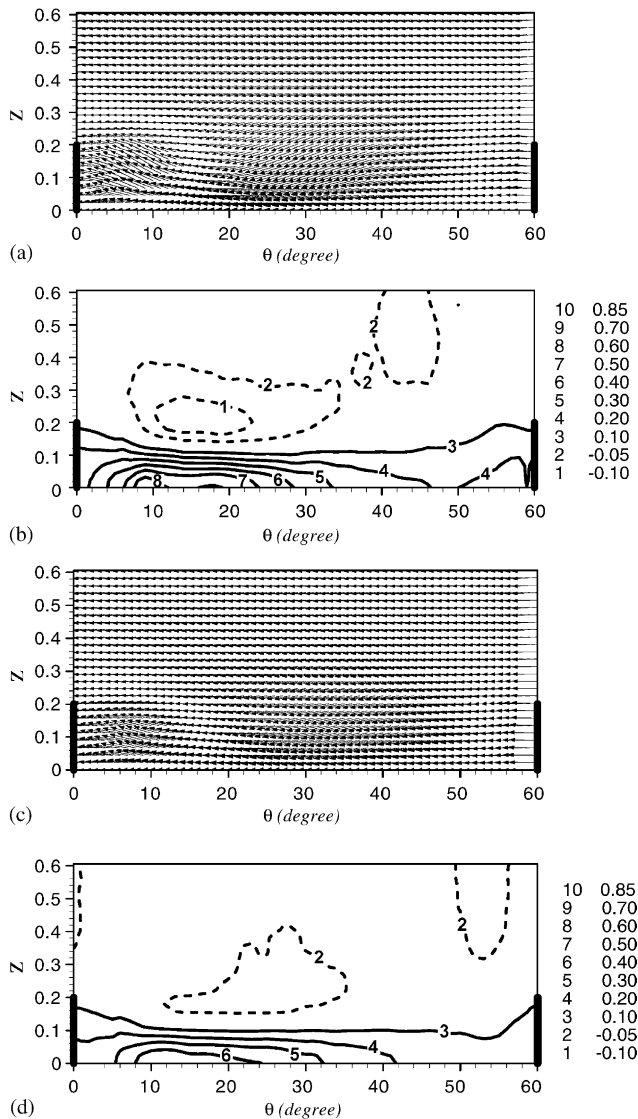

Fig. 3. (a) The in-plane velocity vector plot and (b) the out-of-plane radial velocity contours of the phase-averaged mean flow at $Re = 4300$ for the small tank. (c) The in-plane velocity vector plot and (d) the out-of-plane radial velocity contours at $Re = 63,180$ for the small tank.
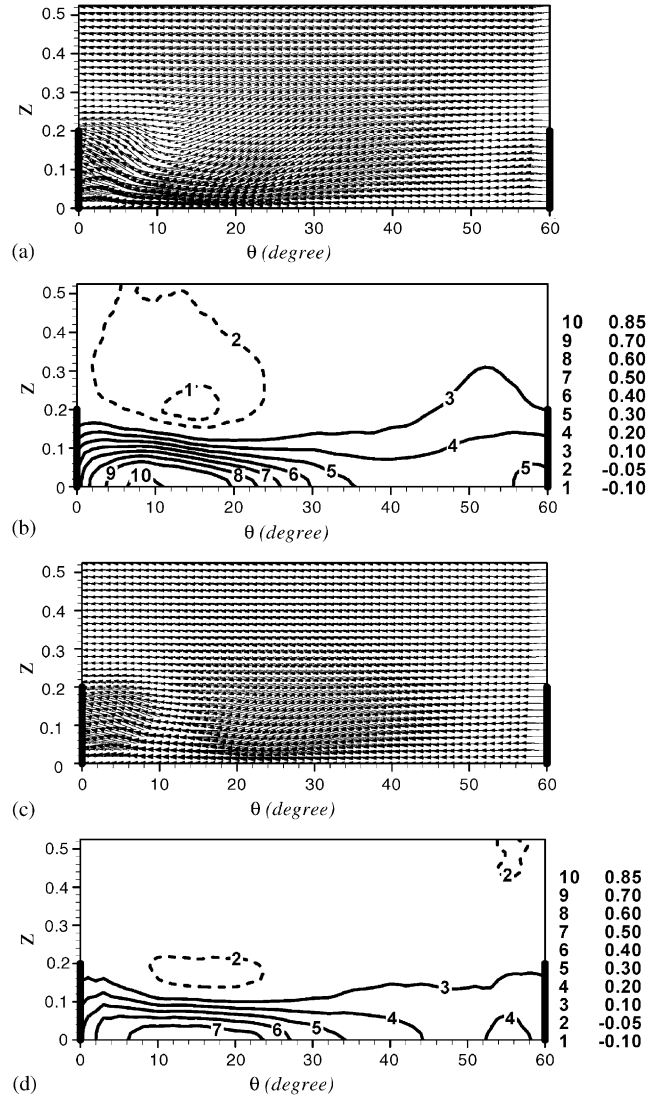

Fig. 4. (a) The in-plane velocity vector plot and (b) the out-of-plane radial velocity contours of the phase-averaged mean flow at $Re = 4299$ for the large tank. (c) The in-plane velocity vector plot and (d) the out-of-plane radial velocity contours at $Re = 62,646$ for the large tank.

tip vortex pair cuts the cylindrical plane at an angle, and its sense of rotation is such that it enhances the radial velocity due to the jet at the midplane ($z = 0$), but opposes the jet sufficiently away from the midplane. In fact, the negative radial velocity and its localized peak around $\theta = 18°$ and $z \approx 0.2$ is a clear signature of the tip vortex. This observation is quite consistent with the recent measurements of Escudie et al. (2004). Fig. 3 (frames c and d) shows the mean flow for the small tank corresponding to a higher Reynolds number of 63,180. Although the in-plane and radial velocity components are qualitatively similar to the low Reynolds number case, measurable quantitative differences can be observed, indicating a Reynolds number effect. For example, the peak (positive and negative) radial velocities are somewhat lower at the higher Reynolds number than at the lower Re. Fig. 4 shows the mean flow results for the large tank at

$Re = 4229$ and 62,646. They are, again, qualitatively comparable to those shown in Fig. 3. Some differences can be observed, in particular, the signature of the tip vortex moves closer to the blade (smaller values of θ), suggesting some difference in the tip vortex location and orientation. Again, a comparison of Fig. 4b with 4d reveals that the intensity of radial velocity appears to decrease with increasing angular velocity of the blade. However, for about the same Reynolds number the radial velocity for the large tank is somewhat stronger than the small tank.

The normalized mean radial, circumferential and axial velocities averaged over θ, $\overline{\langle u_r \rangle}$, $\overline{\langle u_\theta \rangle}$, $\overline{\langle u_z \rangle}$, (overbar indicates θ-average) are shown in Fig. 5 for the small tank. Upon θ-average the effect of tip vortex pairs gets averaged, and the contribution to the mean flow from the jet stands out, being clearly evident as the rapid increase in the radial velocity as the midplane is approached. The weak negative peak in the radial velocity around $z = 0.2$ is due to the tip vortex pair. Such negative radial velocity above and below the blade has been observed in other measurements as well (Escudie and Line, 2003). However, here due to circumferential averaging the negative peak is much weaker than observed in (Escudie and Line (2003). The asymptotic negative radial velocity approached for large z is due to the broad return flow back towards the impeller region. The jet has a strong circumferential component oriented in the direction of blade rotation (note that θ is measured in the direction opposite to blade rotation). At this radial location ($r = 1.06$) the radial component of the jet is larger than the circumferential component. As can be seen in Fig. 5b, as z increases the circumferential velocity approaches a constant value, suggesting a background circumferential flow, which is only weakly dependent on z. The magnitude of the radial velocity steadily decreases with increasing Reynolds number, while the magnitude of circumferential velocity increases with Re. However, a tendency towards Reynolds number independence for these normalized velocity profiles is observed with increasing Reynolds number. The axial velocity component is much weaker in magnitude, and it arises from the jet-induced entrainment and also from the large tank-wide circulation. Although the variation with increasing Re is not monotonic, a tendency towards Reynolds number independence can be observed here, as well.

The above results for the small tank compare favorably with those for the large tank shown in Fig. 6. The jet amplitude for the large tank appears to be slightly stronger than that for the small tank. Apart from this difference, the comparisons of all three components of velocity in Figs. 6 and 5 are quite good, especially in the high Reynolds number range. This observation, along with the differences observed earlier between Figs. 3 and 4, suggests that the tip vortex pairs depend on tank size. This may be due to the critical dependence of tip vortices on the impeller geometry and the small difference in the impellers between the two tanks may be contributing to this small, but noticeable, difference in the tip vortex signatures.
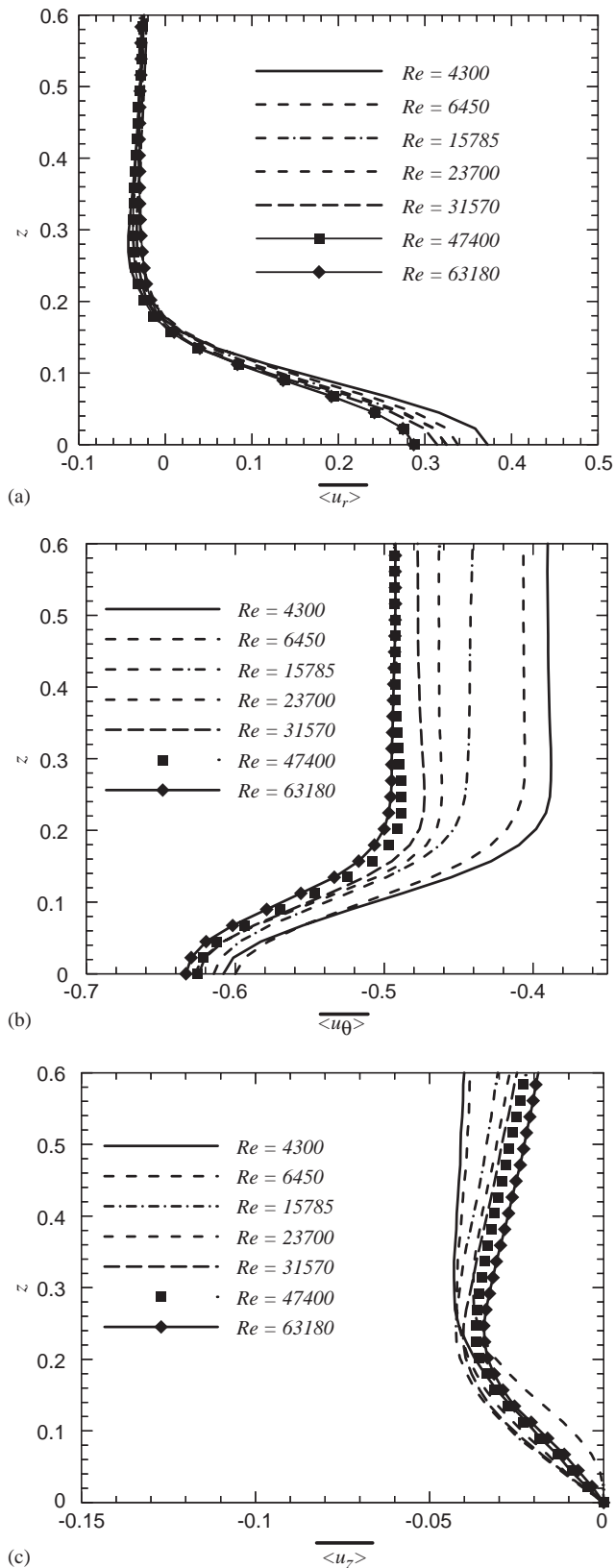

Fig. 5. The normalized phase-averaged mean (a) radial, (b) circumferential and (c) axial velocities averaged over the circumferential direction ($\overline{\langle u_r \rangle}$, $\overline{\langle u_\theta \rangle}$, $\overline{\langle u_z \rangle}$); overbar indicated θ-average) as a function of z for the different Reynolds numbers for the small tank.

(a)

(b)

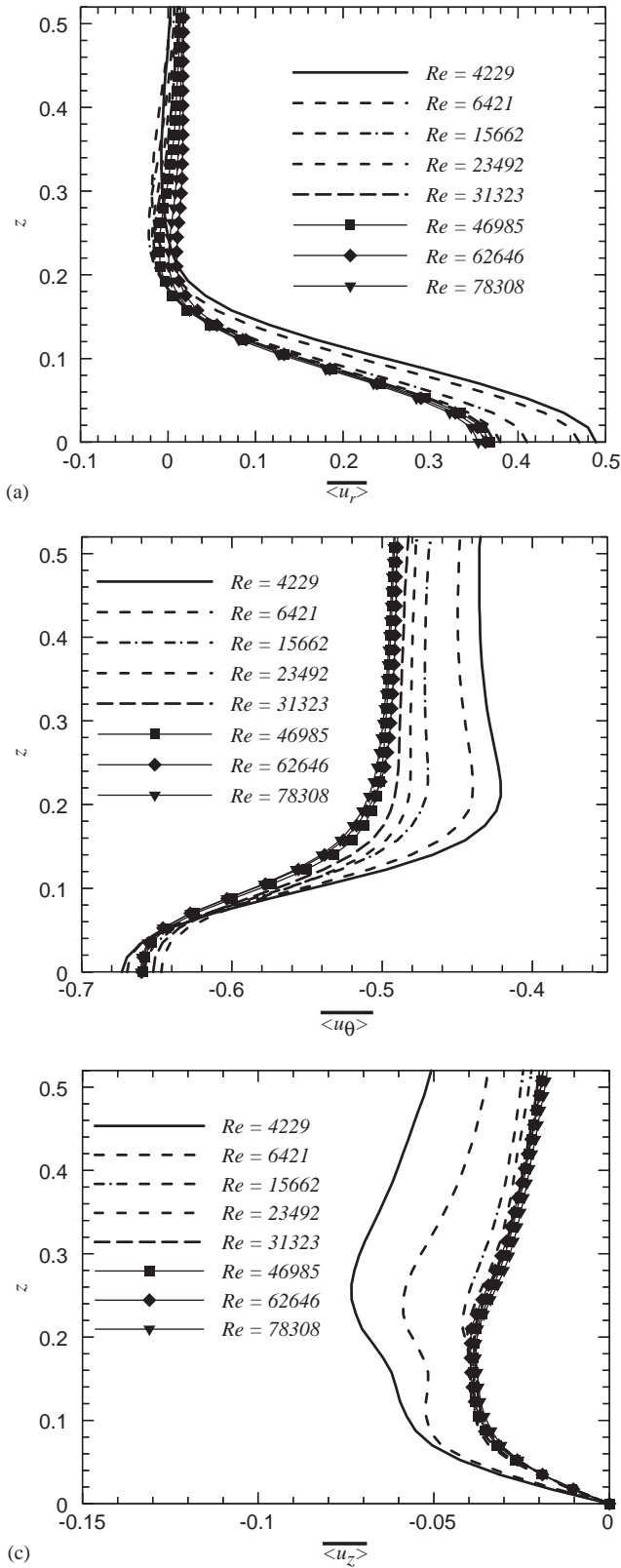(c)
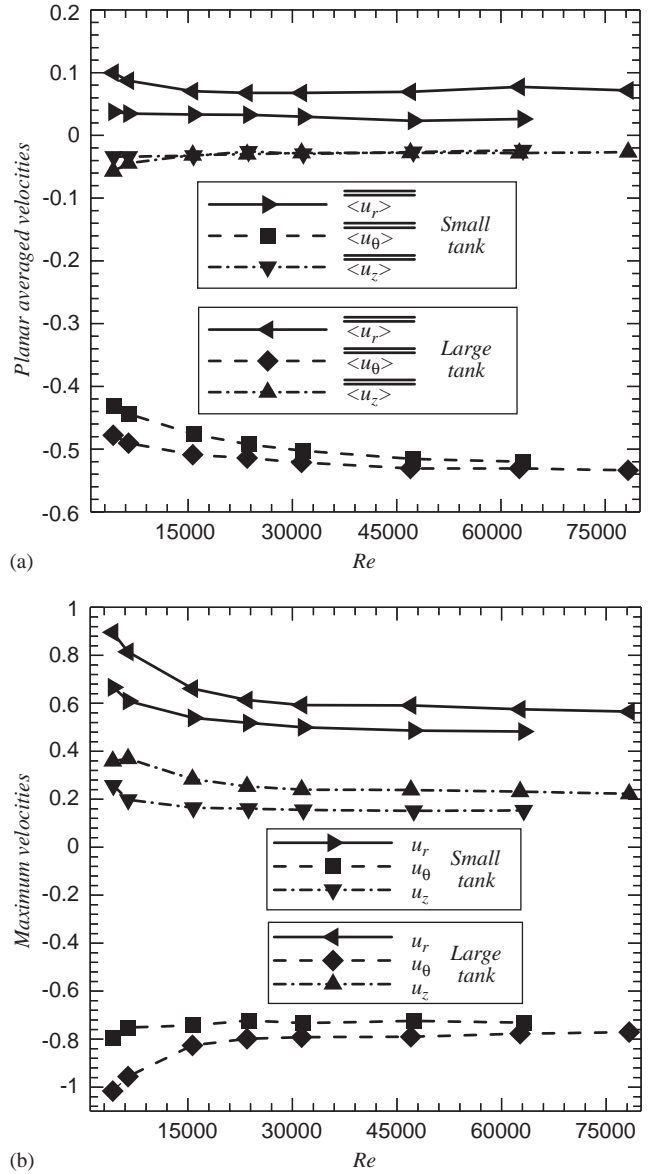
Fig. 6. The same as Fig. 5 for the large tank.

(a)

(b)

Fig. 7. (a) The normalized phase-averaged mean radial, circumferential and axial velocities averaged over the entire θ–z plane ($\overline{\overline{\langle u_r \rangle}}, \overline{\overline{\langle u_\theta \rangle}}, \overline{\overline{\langle u_z \rangle}}$) (the double overbar indicates a planar average) as a function of Reynolds numbers for the two different tank sizes. (b) The maximum (over the θ–z plane) phase-averaged mean radial, circumferential and axial velocities as a function of Reynolds number for the two different tanks.

Fig. 7a shows the normalized mean radial, circumferential and axial velocities averaged over the entire θ–z plane, $\overline{\overline{\langle u_r \rangle}}, \overline{\overline{\langle u_\theta \rangle}}, \overline{\overline{\langle u_z \rangle}}$, (the double overbar indicates a planar

average) as a function of Re for the two different tank sizes. Above a Reynolds number of about 15,000 the results for all three components of velocity show very little variation. The average velocities in the two different tanks are in reasonable agreement as Re increases, except for the radial component of velocity. The scaling of the maximum value of $\langle u_r \rangle$, $\langle u_\theta \rangle$ and $\langle u_z \rangle$, maximum over the θ–z plane, is shown in Fig. 7b as a function of Re for the two different tank sizes. Even the axial component of velocity shows a weak dependence on tank size in its asymptotic value appropriate at large Re. These differences in the results for the

two tanks must have their origin in the subtle departures from a perfect geometric scaling of the two impellers.

Here, it should be pointed out that in some of the earlier efforts (van der Molen and van Maanen, 1978; Ducoste et al., 1997) the comparison of different tank sizes is performed while maintaining the volume averaged mean dissipation rate to be the same. Since dissipation scales as $N^3 D^2$, it can be expected to go as Re^3 in a fixed tank with increasing blade tip velocity, or as D^{-4} with increasing tank size for a fixed Re. Fixed dissipation rate implies that with increasing tank size one must consider increasing blade tip velocity such that $Re \propto D^{4/3}$. The good degree of Reynolds number independence exhibited in both the tanks in Fig. 7 suggests that the lack of perfect collapse between the two tanks will persist even when compared on the basis of constant volume averaged mean dissipation rate.

It is interesting to note that for the large tank at the lowest Re considered the maximum circumferential velocity exceeds the blade tip velocity (possibly due to the tip vortex influence). With increasing Reynolds number, however, the magnitude of peak circumferential velocity is reduced below the blade tip velocity. While the peak radial velocity remains comparable to the peak circumferential velocity, in terms of the surface-averaged mean, the radial velocity is an order of magnitude weaker than the circumferential component. This is to be expected, since a radial return flow is required to satisfy continuity, and as can be seen in Figs. 5 and 6, even a short distance away from the impeller (for $|z| > 0.2$) the radial velocity is negative.

3.2. Decomposition of mean flow

The theoretical model presented in Yoon et al. (2001), considered the impeller-induced phase-averaged mean flow as a superposition of a circumferential flow, a circular jet and a pair of tip vortices associated with each impeller blade. Their superposition for the mean flow, in a frame of reference rotating with the blade, can be expressed as

$$\mathbf{u}(r, \theta, z) = \mathbf{u}_c(r, z) + \mathbf{u}_{\text{jet}}(r, z) + \mathbf{u}_{\text{vort}}(r, \theta, z), \qquad (1)$$

where $\mathbf{u}_c$ is a purely circumferential flow. Its strongest variation is along the radial direction, and it is only weakly dependent on z. In the laboratory frame of reference the time-averaged flow is axisymmetric as the effect of the impeller blades gets averaged out and remains invariant to θ. The effect of the impeller blades and the associated tip vortices can be better accounted for in the mean flow in a frame of reference that rotates with the blades. In the rotating frame, the blades remain fixed in position and the time-averaged mean flow is periodic over the 60° sector between the blades. Thus, the above superposition in the rotating frame of reference allows for the description of a complex impeller-induced flow, with all three (radial, circumferential and axial) components of velocity strongly dependent on all three coordinate directions.

In the case of a Rushton turbine the jet flow slowly changes direction from a circumferential direction to a more radial direction with increasing radial distance from the axis (Kolar et al., 1982, 1984; Kresta and Wood, 1991). Thin shear layer theory can be applied and an approximate self-similar solution can be obtained for the jet (see Yoon et al., 2001). At any radial distance, r, from the axis of the tank the self-similar jet is directed at an angle $\theta_{\text{jet}} = \cos^{-1}(\sqrt{r^2 - a^2}/r)$ to the radial direction and the jet velocity along this direction is given by

$$u_{\text{jet}} = \frac{A}{r^{1/2}(r^2 - a^2)^{1/4}} \left\{ 1 - \tanh^2 \left(\frac{\sigma z}{\sqrt{r^2 - a^2}} \right) \right\}. \qquad (2)$$

The jet flow is fully characterized by three parameters: A—a measure of the jet momentum, $1/\sigma$—a measure of the jet thickness and a—the virtual origin.

The tip vortices are generated from the roll-up of the shear layers as flow accelerates around the rotating impellers (van der Molen and van Maanen, 1978; Stoots and Calabrese, 1995; Yianneskis et al., 1987). The tip vortices are at their peak strength close to the impellers and weaken as they extend radially out into the tank. The backbone of the tip vortex pair is curved backwards in the circumferential direction opposite to the direction of rotation. The tip vortices remain coherent, and as shown in the recent large eddy simulations (Yoon et al., 2002), at any instant in time they extend over 180° along the circumferential direction. While their head remains anchored behind the rotating blades, their tail oscillates in position over time as they extend into the tank. Upon time averaging, a tip vortex pair's extent into the tank is somewhat reduced to about 60° along the circumferential direction. Yoon et al. (2001) observed that the strength and size of the average tip vortex pair changes along its backbone.

The full details of the tip vortex pair along its entire backbone cannot be obtained from the present PIV measurements. But, velocity fields such as those shown in Figs. 3 and 4 can be used to characterize the tip vortex pair as it cuts through the cylindrical plane $r \approx 1.06$. On this plane the location of tip vortex pair is characterized by θ_v, the angle between the vortex center and the nearest blade and $\pm z_v$, the axial location of the vortex centers from the midplane. The vortex backbone cuts the cylindrical plane, $r \approx 1.06$, at an oblique angle and thus the local orientation of the vortex pair is additionally characterized by the angle, ϕ_v, between the backbone and the local radial direction. To good approximation the vortex pair can be taken to be viscous vortices. Therefore the azimuthal velocity (different from circumferential or θ component of velocity) in the neighborhood of any of the vortex on a plane normal to the vortex backbone can be expressed as

$$u_{\text{azim}} = \frac{\Gamma}{\xi}[1 - \exp(-\delta \xi^2)], \qquad (3)$$

where ξ is the normal (shortest) distance from the vortex backbone to the point at which the velocity is evaluated. The other two parameters that characterize the vortex

Table 2
The vortex parameters: $\pm z_v$, the axial location of vortex center from the midplane, θ_v, the angle between the vortex center and the nearest blade, ϕ_v, the angle between the vortex backbone and the local radial direction at the point where it intersect the cylindrical plane

$Re = ND^2/v$	$\pm z_v$	θ_v (∘)	ϕ_v (∘)
4300	0.08	18	56.3
6450	0.08	19	56.43
15,785	0.085	19	52.23
23,700	0.085	24	55.6
31,570	0.087	21	57.87
47,400	0.087	21	58.63
63,180	0.087	21	59.35
4229	0.087	12	48.41
6421	0.091	12	51.94
15,662	0.092	15	57.1
23,492	0.093	16	57.15
31,323	0.094	16	57.5
46,985	0.096	15	59.27
62,646	0.09	13	58.4
78,308	0.09	16	59.61

are: Γ, the strength (or circulation) of the vortex and, $1/\sqrt{\delta}$, the vortex core diameter. The above five parameters completely characterize the effect of the tip vortices, at least in the neighborhood of the impeller.

3.3. Tip vortex scaling

The influence of circumferential flow and circular jet can be subtracted from the experimental measurements to isolate the contribution from the tip vortex pairs. Following a procedure similar to that in Yoon et al. (2001) we extract the parameters associated with the tip vortex pair that yield the best match to the experimental measurements. Table 2 shows the location of the tip vortex centers on the cylindrical plane ($r \approx 1.06$) in terms of their axial position ($\pm z_v$) with respect to the midplane and circumferential (θ_v) position measured with respect to the nearest blade in the direction opposite to the direction of impeller rotation. In nondimensional terms, the axial location of the vortex center about the midplane remains nearly independent of Reynolds number and shows a slight increase with the size of the tank. The nondimensional total height of the blade is 0.4; thus the vortices are located roughly halfway between the center plane and the top or bottom edge of the blade. The circumferential location of the vortex center also does not show a strong dependence on Reynolds number, however, with increasing tank size the vortex center is observed to move closer to the blade.

Van't Riet and Smith (1975) observed the curvature of the vortex trajectory and as a result the circumferential location of the vortex, θ_v, to decrease initially with Reynolds number. However, for Re greater than about 5000 they observed the vortex trajectory to be nearly Reynolds number independent within the uncertainties of the experimental measurement. The Reynolds number range for present investigation is in general larger than 5000. Nevertheless, the slight increase in θ_v with increasing Reynolds number seen in Table 2, opposes the trend observed by Van't Riet and Smith (1975).

Also shown in Table 2 is the angle, ϕ_v, the vortex backbone makes with the radial direction at the point where it intersects the cylindrical plane ($r \approx 1.06$). For both the small and large tanks the angle, ϕ_v, shows a slight increase with increasing Reynolds number, indicating a more circumferential orientation for the tip vortex trajectory at higher Re. This result is consistent with the observed slight increase in θ_v with Reynolds number. At lower Reynolds numbers the tip vortex backbone is directed closer to the radial direction in the large tank than in the small tank. However, as Re increases to larger values, for both tanks ϕ_v appears to asymptote to an angle of about 60°. Within the impeller swept volume (for $r < 1$) on the leeward side of the rotating blades the tip vortex pairs lie parallel to the blade and have a near radial orientation. Within a short distance away from the blade tip the tip vortices sharply curve backwards. As can be seen from Table 2, for all cases considered ϕ_v is noticeably higher than 45°, indicating a more circumferential local orientation for the vortex backbone.

Fig. 8a shows a plot of the nondimensional vortex strength as a function of Re for the two different tanks considered (nondimensionalized by $\pi ND^2/2$). The nondimensional vortex strength decreases with increasing Re, with the rate of decrease higher at lower Re. A tendency towards Reynolds number independence can be inferred, although even for the highest Reynolds number considered this asymptotic state is not yet attained for the large tank. From the figure it appears that for both tanks an asymptotic value of about 0.017 may be appropriate for Re greater than about 10^5. The above scaling indicates that the relative importance of the vortex pair is higher at lower Reynolds number and levels off at higher Reynolds numbers. The observed dependence of nondimensional vortex strength with tank size may be due to the subtle differences in the actual impellers employed for the small and large tanks. Interestingly the measurements of van der Molen and van Maanen (1978) also shows a dependence of tip vortices on tank size.

The measure of vortex size, $1/\sqrt{\delta}$, is shown in Fig. 8b. For the small tank the nondimensional size decreases slightly from a value of about 0.085 at lower Re to an asymptotic value of about 0.07 with increasing Re. The relative size of the vortex is somewhat small for the large tank. With increasing Re the asymptotic value of $1/\sqrt{\delta}$ for the large tank is about 0.055. The large tank is twice bigger than the small tank, and therefore in dimensional terms the vortex size for the large tank is only about factor 1.5 bigger than that for the small tank.

3.4. Scaling of the circular jet

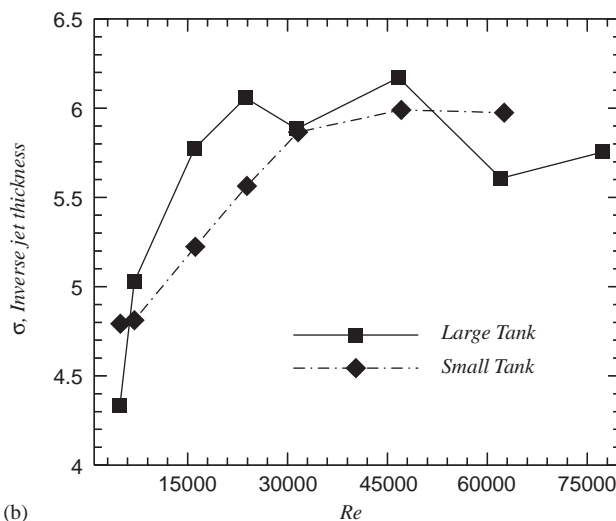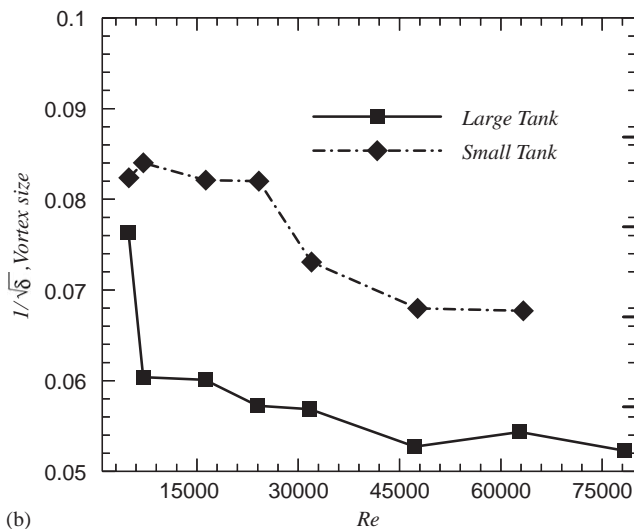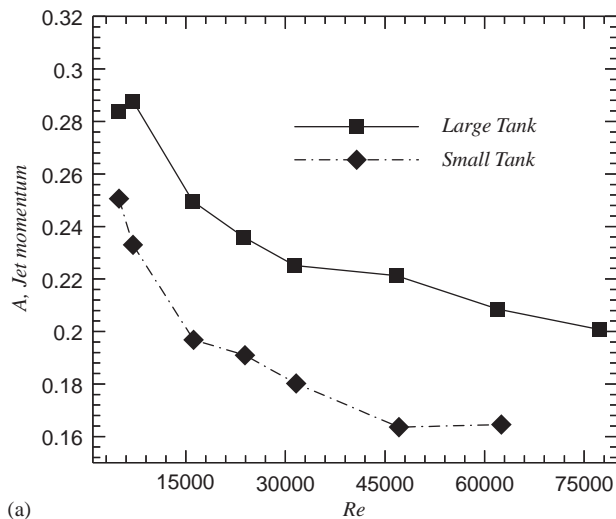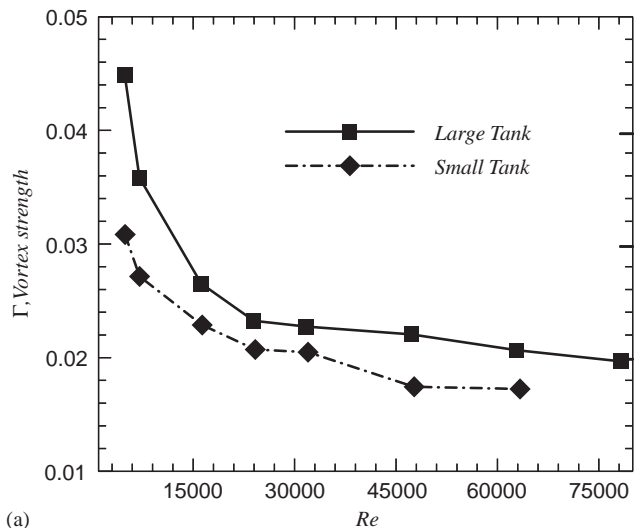Fig. 9a shows the nondimensional jet momentum parameter, A (nondimensionalized by $\pi ND^2/2$) for varying

Fig. 8. (a) The scaling of nondimensional vortex strength, Γ and (b) the nondimensional vortex size, $1/\sqrt{\delta}$, as a function of Reynolds numbers for the two different tank sizes.

Reynolds number for the two different tanks. For the small tank an asymptotic constant value of about 0.165 is reached for *Re* greater than about 45,000. For the large tank a complete Reynolds number independence is not observed even for the largest Reynolds numbers considered. However, a tendency towards Reynolds number independence may develop at *Re* exceeding 75,000. The strength of the jet in nondimensional terms is observed to be somewhat stronger for the large tank and that is consistent with the differences between the two tanks seen in Figs. 5 and 6.

Fig. 9b shows that the inverse jet thickness, σ, for the two different tanks exhibits better collapse than the jet momentum. The nondimensional jet thickness decreases with increasing Reynolds number at lower Reynolds numbers, and above a Reynolds number of about 30,000, the jet thickness appears to level off and become nearly independent of *Re*. The asymptotic value of nondimensional inverse jet
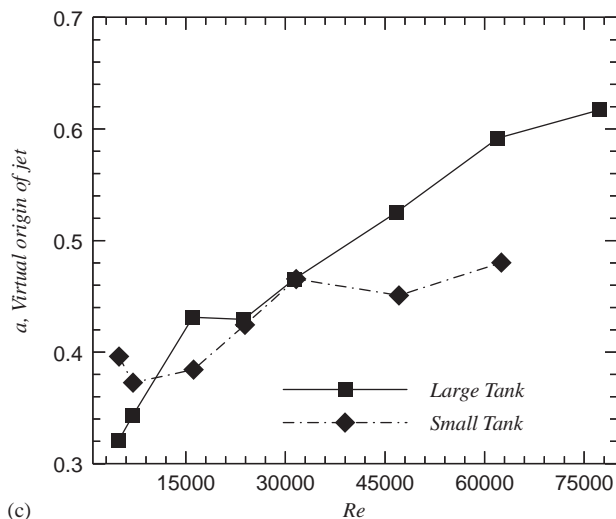

Fig. 9. (a) The scaling of the nondimensional jet momentum, A; (b) the inverse jet thickness, σ; and (c) the virtual origin, a, as a function of Reynolds number for the two different tanks.

thickness for the two tanks is, $\sigma_{asym} \approx 6$. Note that the impeller radius is the length scale used in the nondimensionalization and hence, in dimensional terms, the jet width is about one-sixth (0.166) of the impeller radius. This can be compared with the height of the impeller blade, which is approximately 0.4 times the impeller radius.

Fig. 9c shows the variation of virtual origin, a, with respect to Re for the two different tanks. A similar trend is exhibited for both tanks with the virtual origin progressively increasing with increasing Reynolds number. The rate of increase is, however, somewhat larger for the large tank. For both tanks a clear asymptotic behavior is not reached even for Reynolds number as large as 75,000. The approach of the virtual origin closer to blade tip ($r = 1$) suggests that as Reynolds number increases the importance of circumferential component of jet velocity increases at the expense of the radial component, which is again consistent with the velocity profiles shown in Figs. 5 and 6. However, as pointed out earlier, at the radial location of velocity measurement the radial component of the jet is somewhat stronger than the circumferential component over the entire Reynolds number range considered.

3.5. Scaling of the circumferential flow

At the plane of interpolated experimental mean flow data (at $r \approx 1.06$) the jet is neither completely radial nor purely circumferential. The jet flow has a circumferential component, which for increasing Reynolds number can be inferred to be slightly larger for the large tank than for the small tank (owing to the somewhat larger value of a for the large tank). This contribution alone does not fully account for the measured θ-velocity and the circumferential impeller-induced flow, $\mathbf{u}_c$, is defined to account for the balance (note that $\mathbf{u}_c$ is directed purely in the circumferential direction). Figs. 10a and b show the circumferential flow, $\mathbf{u}_c$, as a function of axial location at $r \approx 1.06$ for the varying Reynolds numbers for the two different tanks. Only the region close to the impeller ($z < 0.5$), where the measurement is made, is shown. For comparison the blade extends from $-0.2 < z < 0.2$, while the tank from bottom to top is given by $-3 < z < 3$.

In the rotating frame of reference the impeller-induced circumferential flow is directed opposite to the direction of blade rotation. The circumferential flow, $\mathbf{u}_c$, is weakly dependent on the axial direction for the small tank and only slightly more dependent in the large tank, close to the impeller blade. A clear Reynolds number dependence occurs in both the tanks. The magnitude of the circumferential flow initially increases with increasing Reynolds number, but, above a Reynolds number of about 45,000 saturation occurs. For the small tank the magnitude of the nondimensional circumferential flow increases from a value of about 0.4 at $Re = 4300$ to a value of about 0.5 at the higher Reynolds number. For the large tank the magnitude of increases from a value of about 0.44 at $Re = 4229$ to a value of about 0.5 at the
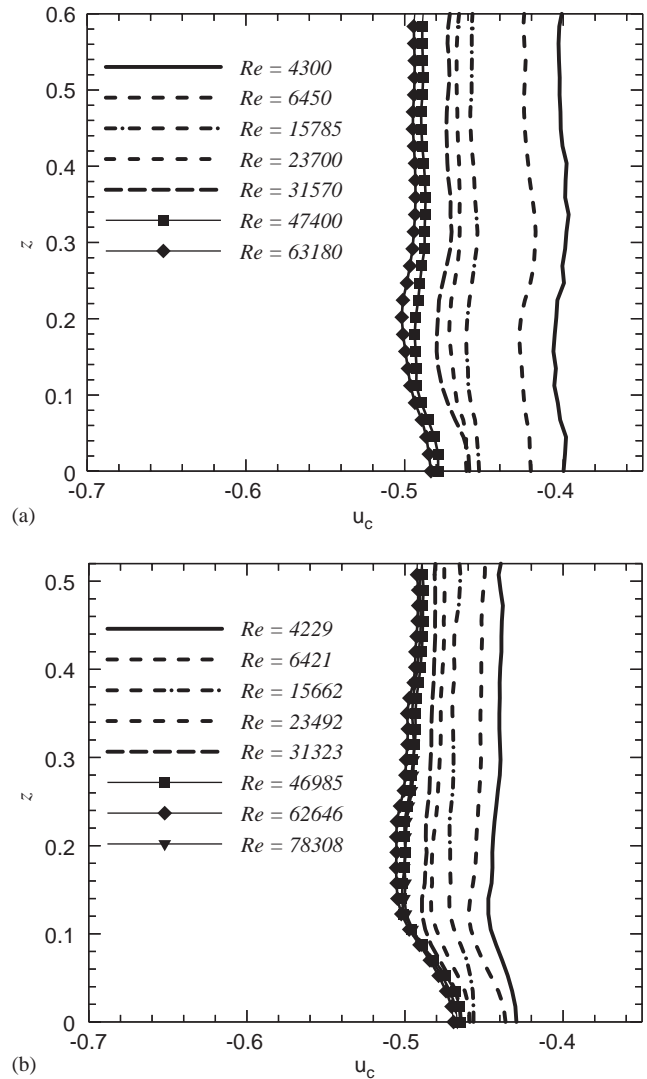

Fig. 10. The circumferential flow, $\mathbf{u}_c$, as a function of axial location at $R \approx 1.06$ for the varying Reynolds numbers for (a) the small tank and (b) the large tank.

highest Reynolds number considered. Thus, at sufficiently large Reynolds number the circumferential flow scales with the blade-tip velocity.

On the cylindrical surface of interpolated mean velocity the effect of tip vortices is the strongest on the leeward side of the blade (that is for small values of θ). On this surface the velocity field at large values of θ is dominated by the jet and the circumferential flow. Thus the efficiency of the jet and the circumferential flow models in capturing the measured mean flow variation can be evaluated from the data at large θ. As an example, Fig. 11a shows the experimental mean radial, circumferential and axial velocity components as a function of z at $\theta = 55°$ for the small tank at $Re = 23,700$. The corresponding result for the large tank at $Re = 23,492$ is shown in Fig. 11b. The excellent representation for the circumferential velocity component is due to the fact that
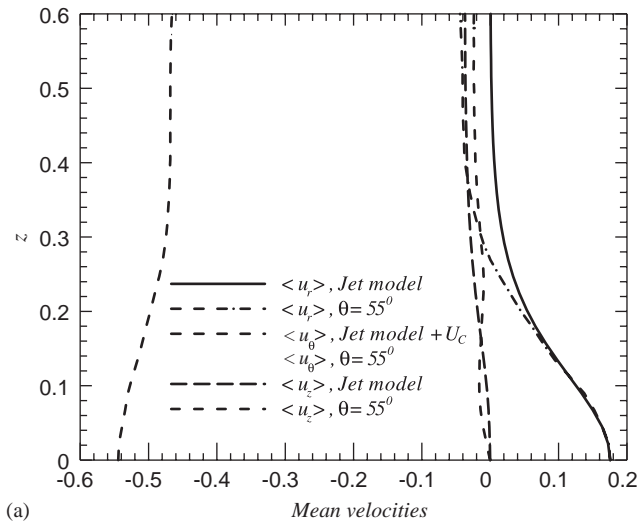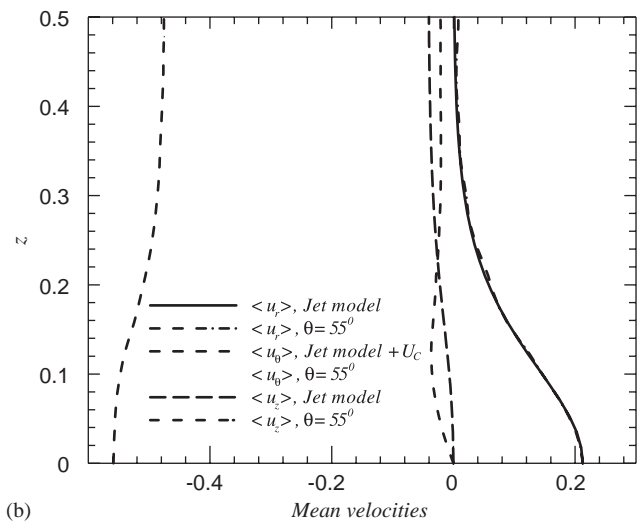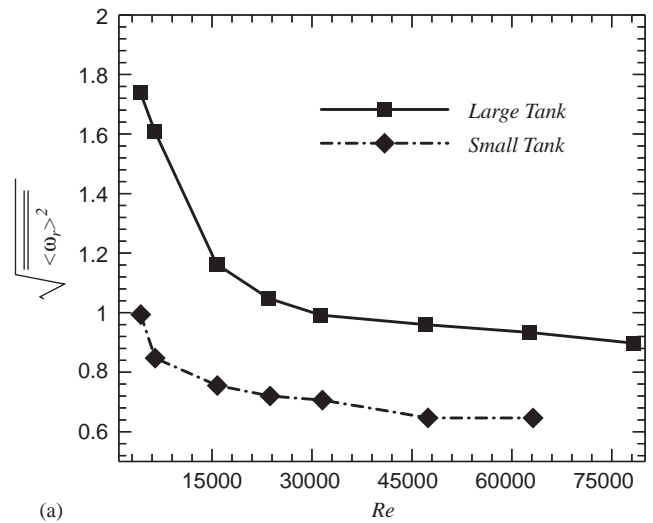
Fig. 11. The experimental phase-averaged mean radial, circumferential and axial velocity components as a function of z for (a) the small tank at $\theta = 55°$ and $Re = 23{,}700$ and (b) the large tank at $\theta = 50°$ and $Re = 23{,}492$. Also shown for comparison are the corresponding velocities from the theoretical jet model.

Fig. 12. (a) The square-root of surface-averaged mean square vorticity, $\sqrt{\overline{\langle \omega_r \rangle}}$, plotted as a function of Re for the two different tanks, (b) the corresponding trend of the surface maximum radial vorticity.
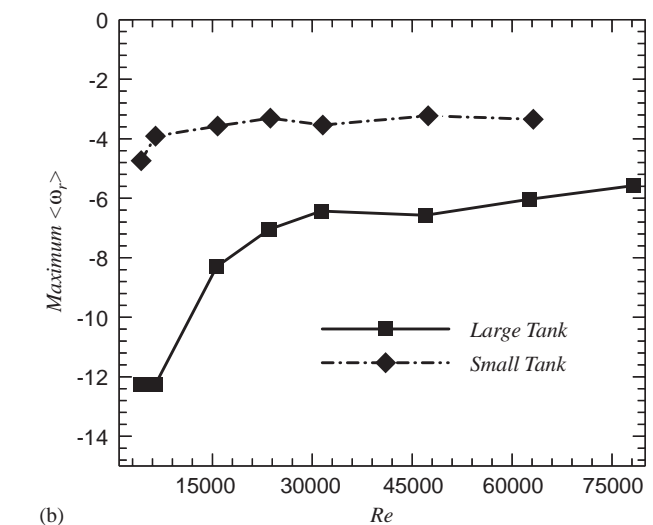
the circumferential component, $\mathbf{u}_c$, has been defined to yield the best agreement for large θ. Good representation can be observed for the radial velocity, except the model is constrained to approach zero radial velocity with increasing z, while a small negative radial inflow is observed in the experiment for large z for the small tank. The agreement for the axial velocity is reasonable; however the magnitude of axial velocity is significantly smaller than the other two components. Similar comparison has been made for both the tanks over the entire range of Re.

3.6. Vorticity and dissipation scaling

The measurement of all three components of the mean velocity on three parallel planes allows for accurate evalu-

ation of all components of the mean velocity gradient and thus vorticity and dissipation fields associated with the mean flow. Here we will investigate the scaling of both vorticity and dissipation for the two tanks. The phase-averaged mean radial vorticity can be defined in terms of the mean flow as

$$\langle \omega_r \rangle = \frac{1}{r} \frac{\partial \langle u_z \rangle}{\partial \theta} - \frac{\partial \langle u_\theta \rangle}{\partial z}. \qquad (4)$$

The square-root of surface-averaged mean square vorticity, $\sqrt{\overline{\langle \omega_r \rangle}}$, as a function of Re for the two different tanks is shown in Fig. 12a and the corresponding trend of the surface maximum radial vorticity is shown in Fig. 12b. Compared to the mean flow the approach to Reynolds number independence is delayed for the case of mean vorticity, which is dictated more by the smaller scales of motion. For the small tank an approximate Reynolds number independent
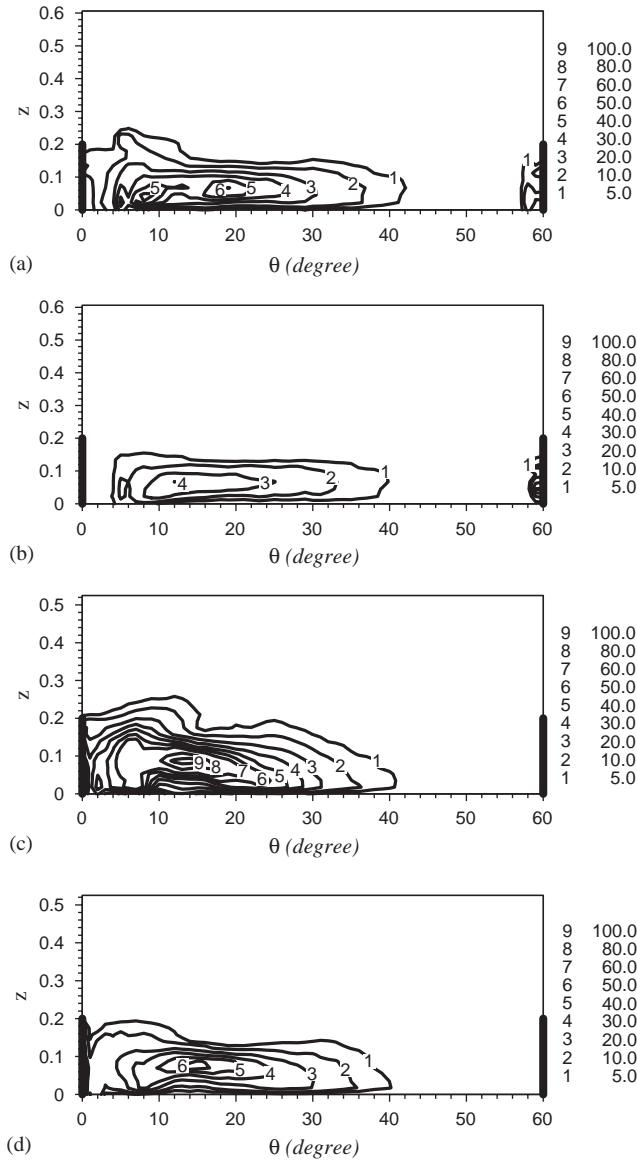
(a)

(b)

(c)

(d)

Fig. 13. Contours of dissipation associated with the mean velocity plotted on the θ–z plane at $R \approx 1.06$ for the small tank at (a) $Re = 4300$, (b) $Re = 63{,}180$ and for the large tank at (c) $Re = 4229$ and (d) $Re = 78{,}308$.
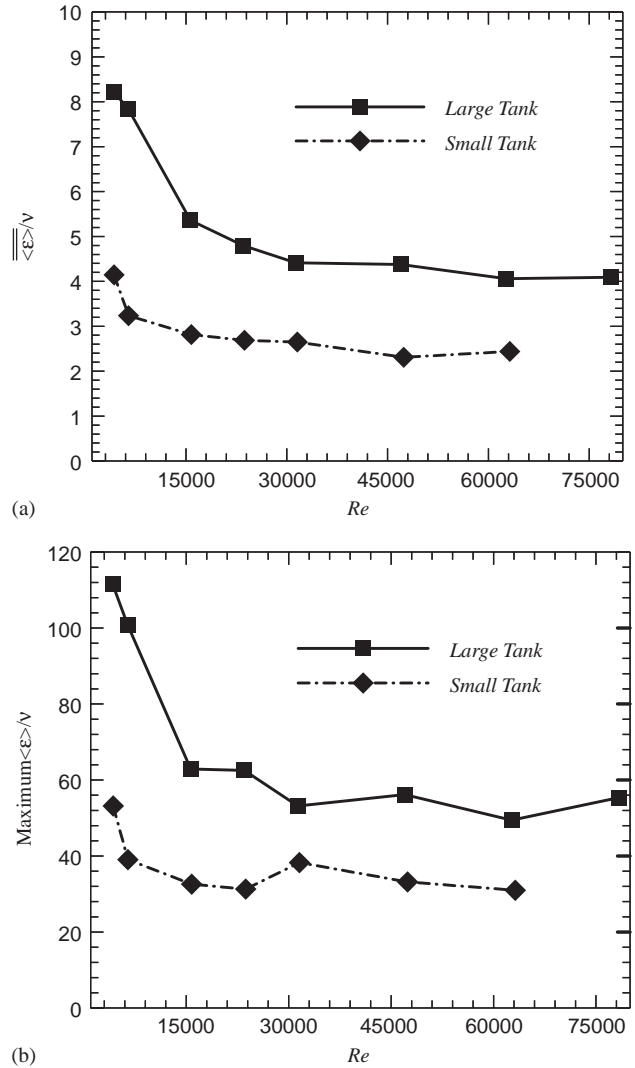

Fig. 14. (a) The surface-averaged dissipation of mean flow plotted as a function of Re for the two different tanks, (b) the corresponding trend of the surface maximum.

behavior can be observed above $Re = 45{,}000$ and for the large tank even a higher Reynolds number needs to be reached before attaining full Reynolds number independence. The difference between the two tanks decreases with increasing Reynolds number, however, a complete collapse is not observed.

Nondimensional dissipation associated with the phase-averaged mean flow can be defined as

$$\varepsilon_m = 2 \frac{\partial \langle u_i \rangle}{\partial x_j} \frac{\partial \langle u_i \rangle}{\partial x_j}, \tag{5}$$

where all the nine components of the gradient of the mean velocity field can be obtained from the measurements on the three vertical plane. The resulting dissipation can then be interpolated onto the cylindrical surface at $r \approx 1.06$. A contour plot of ε_m for the small tank is shown in Figs. 13a and b for the two Reynolds numbers $Re = 4330$ and 63,180. The distribution is similar to that of vorticity and the primary contribution to dissipation from the mean flow appears to be associated with the tip vortex pair. Again the distribution is qualitatively similar for both the Reynolds numbers, however, the magnitude of dissipation decreases with increasing Reynolds number. The corresponding dissipation fields for the large tank for $Re = 4229$ and 78,308 are shown in frames (c) and (d). As with the vorticity field, the dissipation of the mean flow is higher for the large tank.

It must be cautioned that, owing to the quadratic dependence of dissipation on velocity, ε_m does not correspond to the mean dissipation one would obtain from an ensemble average of dissipation computed at individual instances. In the present set of experiments, since the individual realizations

on the different vertical planes are temporally uncorrelated, it is not possible to compute the instantaneous dissipation accurately. ε_m simply represents dissipation associated with the phase-averaged mean flow and its magnitude can be expected to be much smaller than mean dissipation, since the fluctuating small scales play the dominant role in dissipative process. Also there is evidence to show that dissipation increases within the impeller-induced flow from $r = 1$ to about $r = 1.4$ (Escudie and Line, 2003). The surface-averaged dissipation as a function of Re for the two different tanks is shown in Fig. 14a and the corresponding trend of the surface maximum ε_m is shown in Fig. 14b. The approach to Reynolds number independence is similar to that for mean vorticity observed in Fig. 12.

4. Conclusions

Experimental measurements of flow induced by a Rushton turbine in an unbaffled stirred tank have been performed over a wide range of operating speeds. Two different tank sizes were used with water as the working fluid to cover a Reynolds number range of 4000–80,000. Phase-locked stereoscopic PIV measurements were made on three different vertical planes near the impeller to obtain all three components of the impeller-induced flow. Instantaneous realizations were averaged to obtain the phase-averaged velocity on a 60° sector of a cylindrical plane of nondimensional radial location, $r \approx 1.06$, just beyond the blade tip radius. Data on this cylindrical surface dictates the flow in the interior of the tank. Hence, the Reynolds number scaling of this velocity data can serve as a proxy for the Reynolds number scaling of the entire flow. The phase-averaged velocity is dependent on both θ and z, from which θ- and surface-averaged mean velocities are deduced.

All three components of the mean velocity are observed to scale with the blade tip velocity beyond a Reynolds number of about 15,000, in agreement with the findings of previous researchers. The phase-averaged mean flow was decomposed into circumferential, jet and tip vortex elements and the parameters associated with the tip vortex pairs and the circular jet were extracted from the experimental measurements. It is observed that the nondimensional jet and tip vortex strength appears to become Reynolds number independent only at large Re. The thickness of the jet appears to scale with the dimensions of the impeller above a modest Reynolds number of about 20,000; however the diameter of the tip vortex does not appear to scale similarly. The virtual origin of the circular jet, however, shows only a slow tendency towards Reynolds number independence. In the case of tip vortex pairs, the location of their centers on the plane of mean flow measurement ($r \approx 1.06$) remains independent of Re and the tip vortex orientation (with respect to the radial direction), quickly approaches an asymptotic value of about 60° with increasing Reynolds number.

The distribution of dissipation illustrates the importance of the tip vortex contribution to the mean flow. The spatial compactness of the tip vortex pairs contributes to higher gradients and thus to gradient dependent quantities such as dissipation. Reynolds number independence for the nondimensional dissipation is observed above a Reynolds number of about 45,000 and the difference between the small and large tanks persist even at the higher Reynolds numbers.

The most significant finding of the study is the extreme sensitivity of the flow within the tank to small geometric details of the impeller. The small and large tanks used in this study were geometrically similar. The Rushton turbine was also geometrically scaled from the small to the large tank; however, small differences exist between the two. The blade and disk thickness were not perfectly scaled and similarly small differences existed in blade length. If the two tanks were geometrically similar in every respect then Re is the only controlling parameter (since free surface was avoided with a lid, Froude number is not relevant in the present case). The persistent difference in the mean velocity that exists between the small and the large tanks even at asymptotically large Reynolds numbers (see Fig. 7), can only be attributed to the small deviations in the scaling of the impeller. These results suggest a sensitive dependence of even the mean flow to the geometric details of the impeller. The main conclusion to be drawn is that scale-up will not work well unless *all* aspects of the turbine blade are scaled perfectly. In most industrial scale-up from small laboratory to large production sized tanks it is conceivable that a perfect geometric scaling is often not realized. Based on present results, this will certainly be a contributing factor to lack of a consistent scaling behavior.

References

Costes, J., Couderc, J.P., 1988. Study by laser Doppler anemometry of the turbulent flow induced by a Rushton turbine in a stirred tank: influence of the size of the units I: mean flow and turbulence. Chemical Engineering Science 43, 2765.

Derksen, J.J., Doelmann, M.S., Van Den Akker, H.E.A., 1999. Three-dimensional LDA measurements in the impeller region of a turbulent stirred tank. Experiments in Fluids 27, 522.

Desouza, A., Pike, R.W., 1972. Fluid dynamics and flow patterns in stirred tanks with a turbine impeller. Canadian Journal of Chemical Engineering 50, 15.

Dong, L., Johansen, S.T., Engh, T.A., 1994. Flow induced by an impeller in an unbaffled tank—I. Experimental. Chemical Engineering Science 49, 549.

Ducoste, J.J., Clark, M.M., Weetman, R.J., 1997. Turbulence in flocculators: effect of tank size and impeller type. A.I.Ch.E. Journal 43, 328.

Escudie, R., Line, A., 2003. Experimental analysis of hydrodynamics in a radially agitated tank. A.I.Ch.E. Journal 49, 585.

Escudie, R., Bouyer, D., Line, A., 2004. Characterization of trailing vortices generated by a Rushton turbine. A.I.Ch.E. Journal 50, 75.

Hill, D.F., Sharp, K.V., Adrian, R.J., 2000. Stereoscopic particle image velocimetry measurements of the flow around a rushton turbine. Experiments in Fluids 29, 478.

Kemoun, A., Lusseyran, F., Mallet, J., Mahousat, M., 1998. Experimental scanning for simplifying the model of a stirred-tank flow. Experiments in Fluids 25, 23.

Kolar, V., Filip, P., Curev, A.G., 1982. The swirling radial jet. Applied Scientific Research 39, 329–335.

Kolar, V., Filip, P., Curev, A.G., 1984. Hydrodynamics of a radially discharging impeller stream in agitated vessels. Chemical Engineering Communications 27, 313.

Kresta, S.M., Wood, P.E., 1991. Prediction of the three-dimensional turbulent flow in stirred tanks. A.I.Ch.E. Journal 37, 448–460.

Lamberto, D.J., Alvarez, M.M., Muzzio, F.J., 1999. Experimental and computational investigation of the laminar flow structure in a stirred tank. Chemical Engineering Science 54, 919.

Mahouast, M., Cognet, G., David, R., 1989. Two component LDV measurements in a stirred tank. A.I.Ch.E. Journal 35, 1770.

Montante, G., Lee, K.C., Brucato, A., Yianneskis, M., 1999. An experimental study of double-to-single-loop transition in stirred vessels. Canadian Journal of Chemical Engineering 77, 649.

Schaffer, M., Hofken, M., Durst, F., 1997. Detailed LDV measurements for the visualization of the flow field within a stirred tank reactor equipped with a Rushton turbine. Transactions I. Chemical Engineering 75 (part A), 729.

Stoots, C.M., Calabrese, R.V., 1995. Mean velocity field relative to a Rushton turbine blade. A.I.Ch.E. Journal 41, 1.

Sturesson, C., Theliander, H., Rasmuson, A., 1995. An experimental (LDA) and numerical study of the turbulent flow behavior in the near wall and bottom regions in an axially stirred vessel. A.I.Ch.E. Symposium Series 91, 102.

van der Molen, K., van Maanen, H.R.E., 1978. Laser-Doppler measurements of the turbulent flow in stirred vessels to establish scaling rules. Chemical Engineering Science 33, 1161.

Van't Riet, K., Smith, J.M., 1975. The trailing vortex system produced by Rushton turbine agitators. Chemical Engineering Science 30, 1093.

Yianneskis, M., Popiolek, Z., Whitelaw, J.H., 1987. An experimental study of the steady and unsteady flow characteristics of stirred reactors. Journal of Fluid Mechanics 175, 537.

Yoon, H.S., Sharp, K.V., Hill, D.F., Adrian, R.J., Balachandar, S., Ha, M.Y., Kar, K., 2001. Integrated experimental and computational approach to simulation of flow in a stirred tank. Chemical Engineering Science 56, 6635.

Yoon, H.S., Balachandar, S., Ha, M.Y., Kar, K., 2002. Large eddy simulation of flow in a stirred tank. Journal of Fluids Engineering 125, 486.